DRAFT VERSION NOVEMBER 7, 2016
Preprint typeset using LaTeX style emulateapj v. 5/2/11

arXiv:1611.00775v2 [astro-ph.SR] 4 Nov 2016

BINARY SOURCE EVENT MASQUERADING AS PLANET: A NEW MANIFESTATION OF THE BINARY-SOURCE DEGENERACY

Y. K. JUNG[1,21], A. UDALSKI[2,22], J. C. YEE[1,21], T. SUMI[3,23]
AND
A. GOULD[4,5,6], C. HAN[7], M. D. ALBROW[8], C.-U. LEE[4], S.-L. KIM[4], S.-J. CHUNG[4], K.-H. HWANG[4], Y.-H. RYU[4], I.-G. SHIN[1], W. ZHU[5], S.-M. CHA[4,9], D.-J. KIM[4], Y. LEE[4,9], B.-G. PARK[4], R. W. POGGE[5]
(THE KMTNET COLLABORATION)
P. PIETRUKOWICZ[2], S. KOZŁOWSKI[2], R. POLESKI[2,5], J. SKOWRON[2], P. MRÓZ[2], M. K. SZYMAŃSKI[2], I. SOSZYŃSKI[2], M. PAWLAK[2], K. ULACZYK[2]
(THE OGLE COLLABORATION)
F. ABE[10], D.P. BENNETT[11,12], Y. ASAKURA[10], A. BHATTACHARYA[11], M. DONACHIE[13], M. FREEMAN[13], A. FUKUI[14], Y. HIRAO[3], Y. ITOW[10], N. KOSHIMOTO[3], M.C.A. LI[13], C.H. LING[15], K. MASUDA[10], Y. MATSUBARA[10], Y. MURAKI[10], M. NAGAKANE[3], H. OYOKAWA[10], A. SHARAN[13], D.J. SULLIVAN[16], D. SUZUKI[12], P. J. TRISTRAM[17], T. YAMADA[3], T. YAMADA[18], A. YONEHARA[18]
(THE MOA COLLABORATION)
[1]Harvard-Smithsonian Center for Astrophysics, 60 Garden St., Cambridge, MA 02138, USA
[2]Warsaw University Observatory, Al. Ujazdowskie 4, 00-478 Warszawa, Poland
[3]Department of Earth and Space Science, Graduate School of Science, Osaka University, Toyonaka, Osaka 560-0043, Japan
[4]Korea Astronomy and Space Science Institute, Daejon 305-348, Republic of Korea
[5]Department of Astronomy, Ohio State University, 140 W. 18th Ave., Columbus, OH 43210, USA
[6]Max-Planck-Institute for Astronomy, Königstuhl 17, 69117 Heidelberg, Germany
[7]Department of Physics, Chungbuk National University, Cheongju 371-763, Republic of Korea
[8]University of Canterbury, Department of Physics and Astronomy, Private Bag 4800, Christchurch 8020, New Zealand
[9]School of Space Research, Kyung Hee University, Yongin 446-701, Republic of Korea
[10]Institute for Space-Earth Environmental Research, Nagoya University, Nagoya 464-8601, Japan
[11]Department of Physics, University of Notre Dame, Notre Dame, IN 46556, USA
[12]Laboratory for Exoplanets and Stellar Astrophysics, NASA/Goddard Space Flight Center, Greenbelt, MD 20771, USA
[13]Department of Physics, University of Auckland, Private Bag 92019, Auckland, New Zealand
[14]Okayama Astrophysical Observatory, National Astronomical Observatory of Japan, 3037-5 Honjo, Kamogata, Asakuchi, Okayama 719-0232, Japan
[15]Institute of Information and Mathematical Sciences, Massey University, Private Bag 102-904, North Shore Mail Centre, Auckland, New Zealand
[16]School of Chemical and Physical Sciences, Victoria University, Wellington, New Zealand
[17]Mt. John University Observatory, P.O. Box 56, Lake Tekapo 8770, New Zealand and
[18]Department of Physics, Faculty of Science, Kyoto Sangyo University, 603-8555 Kyoto, Japan
Draft version November 7, 2016

ABSTRACT

We present the analysis of the microlensing event OGLE-2016-BLG-0733, which introduces a new type of degeneracy between binary source and planetary perturbations. The light curve of the event exhibits a long-term asymmetric perturbation that would appear to be due to a planet. From detailed analysis of the light curve, however, we find that the perturbation originates from the binarity of the source rather than the lens. This result demonstrates that binary sources with roughly equal-luminosity components can mimic long-term perturbations induced by planets with projected separations near the Einstein ring. The result also signifies the importance of considering various interpretations of planet-like perturbations and of high-cadence observation not only for resolving the degeneracy but also for ensuring the unambiguous detection of the planet.

Subject headings: binaries: general – gravitational lensing: micro

1. INTRODUCTION

Since its proposal as a means to detect compact dark objects in the halo of the Galaxy (Paczyński 1986), microlensing has been applied to various fields of astronomy including planetary science (Mao & Paczyński 1991; Gould & Loeb 1992). Although the number of planets detected by the microlensing method is far less than that of planets detected by other major methods such as the radial velocity and transit methods, microlensing provides a unique tool to find planets that are difficult to detect by other methods, such as planets around faint and dark objects, planets at or beyond the snow line, and planets not gravitationally bound to their host stars (see a detailed review by Gaudi 2012). Therefore, it is complementary to other methods, enabling the comprehensive study of extrasolar planets.

The microlensing signal of a planet is almost always a short-term perturbation on the standard lensing light curve caused by the host of the planet. The signal is usually produced by the passage of the source star close to or over a caustic, which are the locations on the source plane at which the magnification of a point source would be infinite (Erdl & Schneider 1993). The shape, size, and number of caustics vary depending on the separation and the mass ratio between the planet and the host. As a result, planetary perturbations take various forms depending on the characteristics of the planetary system as well as the source trajectory.

Interpretation of the planetary microlensing signal and the characterization of the planetary system require detailed anal-

[21] The KMTNet Collaboration.
[22] The OGLE Collaboration.
[23] The MOA Collaboration.

yses of the signal in the observed light curve. However, accurate interpretation of the signal is often hampered by various scenarios that can mimic the planetary signals. For example, the signals induced from two different binary-lens systems can be similar despite the great difference between their underlying physical characteristics. This degeneracy was presented by Choi et al. (2012) and Bozza et al. (2016), where they showed that short-term anomalies of a subset of lensing light curves could be explained equally well by either a binary lens with roughly equal mass components or a binary with a very large mass ratio (i.e., planetary system). In addition, Gould et al. (2013) showed that microlensing of star spots can give rise to light-curve deviations that very strongly mimic planetary anomalies. Furthermore, the binarity of the source star rather than the lens also can masquerade as planetary signals. Gaudi (1998) pointed out that if a source is a binary star with a large flux ratio between the components and a single lens passes close to both members of the binary source, the light curve can appear to be a normal single-lens curve superposed by a short-term perturbation, which is similar to that of a planetary event. Hwang et al. (2013) showed that this degeneracy could be severe by presenting the light curve of an actually observed event.

In this paper, we present the analysis of OGLE-2016-BLG-0733, which displayed a new and unexpected form of the binary-source degeneracy: the light curve of the event shows a long-term asymmetric perturbation that appears to be due to a planet, but which is actually due to a binary source. In Section 2, we describe the observation of the event, and the light curve modeling is presented in Section 3. In Section 4, we discuss the implications of the results.

2. OBSERVATION

The microlensing event OGLE-2016-BLG-0733 occurred on a star located toward the Galactic bulge with the equatorial coordinates $(\alpha,\delta)_{\rm J2000}$ = ($17^{\rm h}55^{\rm m}54\overset{\rm s}{.}29, -29^\circ50'28''.2$), which corresponds to the Galactic coordinates (l,b) = ($0.369^\circ, -2.388^\circ$). The event was discovered on 2016 Apr 19 UT 19:16 by the Early Warning System (EWS: Udalski et al. 2015) of the Optical Gravitational Lensing Experiment (OGLE: Udalski 2003) survey, which is conducted using the 1.3m Warsaw telescope located at Las Campanas Observatory in Chile. The event was independently discovered by the Microlensing Observations in Astrophysics (MOA: Bond et al. 2001; Sumi et al. 2003) survey. The MOA survey is conducted using the 1.8m telescope located at Mt. John Observatory in New Zealand. In the MOA lensing event list, it is labeled MOA-2016-BLG-202.

In addition to the OGLE and the MOA surveys, the event was also in the footprint of the Korea Microlensing Telescope Network (KMTNet: Kim et al. 2016) survey. The KMTNet survey utilizes three identical 1.6m telescopes that are located at Cerro Tololo Interamerican Observatory in Chile (KMTNet CTIO), South African Astronomical Observatory in South Africa (KMTNet SAAO), and Siding Spring Observatory in Australia (KMTNet SSO). Each of KMTNet telescope is equipped with a 4.0 deg^2 camera. With these instruments, the KMTNet survey covers (12, 40, 80) deg^2 areas of the bulge field with cadences of $(4,\ \geq 1,\ \geq 0.4)$ hr^{-1}, respectively. For the three major fields covered by a 4 hr^{-1} cadence, alternating observations cover the sky with a 6′ offset in order to compensate the gap between camera chips. The event lay in one such pair of fields (BLG02 and BLG42) and thus the

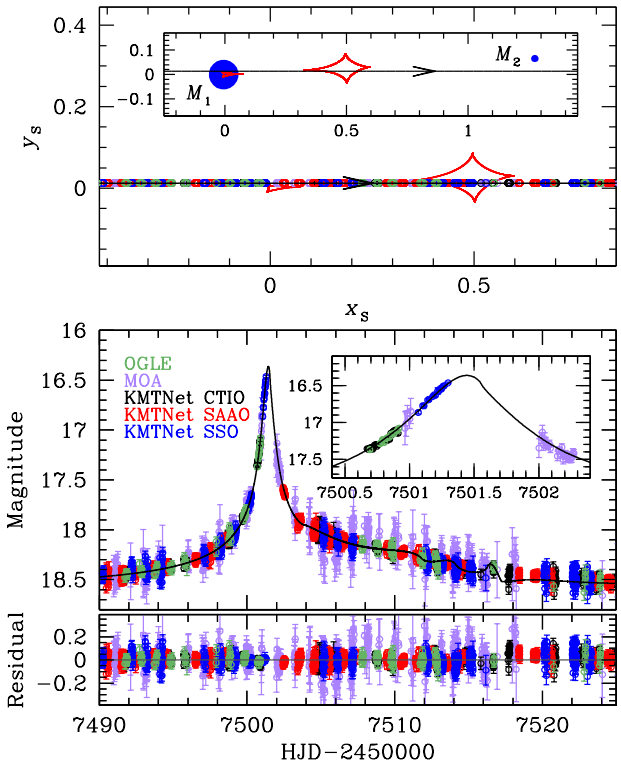

FIG. 1.— Geometry and light curve of the binary-lens model. (1) The upper panel shows the geometry of the binary-lens model. The straight line with an arrow is the source trajectory, red closed concave curves represent the caustics, and blue filled circles (marked by M_1 and M_2) are the binary-lens components. All length scales are normalized by the Einstein radius. The inset shows the general view and the major panel shows the enlarged view corresponding to the light curve of lower panel. The open circle on the source trajectory is the source position at the time of observation whose size represents the source size. (2) The lower panel shows the enlarged view of the anomaly region. The inset shows a zoom of the light curve near HJD′ ∼ 7501.4. The curve superposed on the data is the best-fit binary-lens model.

cadence of the event reached up to 4 hr^{-1}. Combining this feature with its globally distributed telescopes, the KMTNet survey densely and continuously covered the event.

Photometry data used for the analysis were processed using the customized pipelines that are developed by the individual survey groups: Udalski (2003), Bond et al. (2001), and Albrow et al. (2009) for the OGLE, MOA, and KMTNet groups, respectively. These pipelines are based on the Difference Imaging Analysis method (DIA: Alard & Lupton 1998; Woźniak 2000; Albrow et al. 2009).

For the case of KMTNet, data were additionally reduced using the pyDIA [4] software in order to determine the source color. pyDIA is a new modular python package for performing star detection, difference imaging and photometry on crowded astronomical images. For difference imaging, it uses the algorithm of Bramich et al. (2013) with extended delta basis functions that allows independent degrees of control of the photometric and shape changes of the PSF across an image. When available, it uses GPU hardware acceleration for the computationally intensive tasks of difference-imaging and PSF fitting.

A wealth of experience shows that while the error bars reported by microlensing photometry codes are, in general, monotonically related to the true errors, the transformation

[4] http://www2.phys.canterbury.ac.nz/~mda45/pyDIA

TABLE 1
LENSING PARAMETERS

Parameters	Binary-lens	Binary-source
χ^2/dof	12955.8/12347	12411.8/12347
$t_{0,1}$ (HJD′)	7501.570 ± 0.004	7501.374 ± 0.005
$t_{0,2}$ (HJD′)	–	7507.804 ± 0.116
$u_{0,1}$	0.013 ± 0.001	0.015 ± 0.001
$u_{0,2}$	–	0.365 ± 0.033
$t_{\rm E}$ (days)	27.838 ± 0.847	14.428 ± 0.602
s	1.281 ± 0.007	–
q (10^{-3})	3.912 ± 0.258	–
α (rad)	0.051 ± 0.001	–
ρ_* (10^{-3})	8.317 ± 0.392	–
$q_{F,RI}$	–	2.078 ± 0.201
$q_{F,I}$	–	1.853 ± 0.177

NOTE. — HJD′ = HJD − 2450000

from one to the other varies from event to event and from observatory to observatory. To compensate for this effect, we renormalize the error bars of the individual data sets by following the method of Yee et al. (2012) with the equation

$$\sigma'_{i,j} = \sqrt{\sigma^2_{{\rm min},j} + (k_j \sigma_{i,j})^2}, \quad (1)$$

where $\sigma_{i,j}$ is the error on the i-th point from j-th observatory and $\sigma_{{\rm min},j}$ and k_j are the correction parameters for j-th observatory. For each data set, we first adjust $\sigma_{{\rm min},j}$ in order to make the cumulative distribution function of χ^2 sorted by lensing magnification linear. We then rescale the error bars using k_j in order to make χ^2 per degree of freedom (χ^2/dof) unity. Note that the normalization process is conducted based on the best-fit model and we remove 3σ outliers from the model during the process.

3. ANALYSIS

Analysis of the lensing light curve is carried out by conducting modeling of the observed light curve to find the solution of the best-fit lensing parameters. As presented in Figure 1, the light curve of OGLE-2016-BLG-0733 shows deviations from the smooth and symmetric form of an event produced by a single-mass lens. The deviations appear in two regions, one strong anomaly near the peak of the light curve at HJD′(= HJD − 2450000) ∼ 7501.4 and the other weak but long-term anomaly in the falling side of the light curve. Such deviations are broadly consistent with a binary lens.

3.1. *Binary-lens Interpretation*

The light curve produced by a binary lens is complex due to the lack of symmetry in the light-bending surface and the resulting formation of caustic structures. For the basic description of a binary-lens light curve, one needs 7 principal parameters. The first 4 of these parameters describe the relative lens-source motion, including t_0, u_0, $t_{\rm E}$, and α, where the definitions of the parameters t_0, u_0, and $t_{\rm E}$ are the same as those for a single-lens event and α represents the angle between the source trajectory and the binary-lens axis. Since the lens is composed of two masses, one needs a reference position of the lens to define t_0 and u_0. We adopt the center of mass of the binary-lens. Another two parameters describe the binary lens, including the projected binary separation s (normalized to the angular Einstein radius of the lens system, $\theta_{\rm E}$) and the mass ratio q (= M_2/M_1) between the binary-lens components. The last parameter is the source radius ρ_* (normalized to $\theta_{\rm E}$). This parameter is needed to describe the part of the lensing light curve affected by finite-source effects. (see the Appendix of Jung et al. 2015 for graphical presentation of the parameters.)

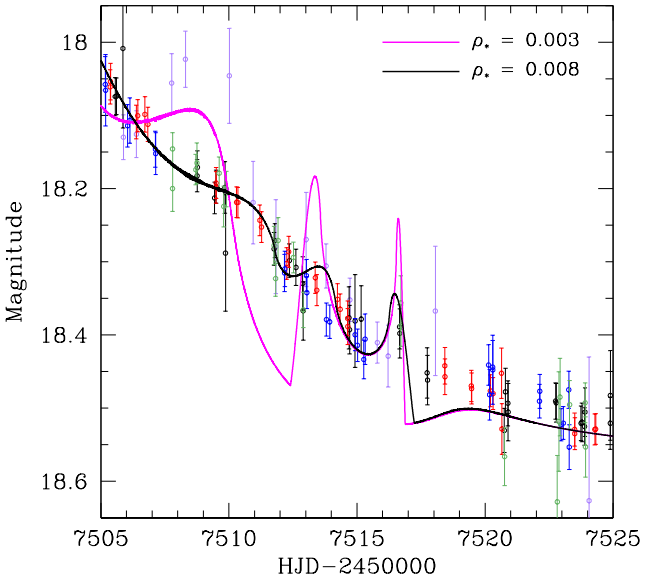

FIG. 2.— Comparison of two binary-lens models in the weak anomaly region. The black and magenta curves represent, respectively, the best-fit model and the same model except with a substantially smaller (and more typical) source size ρ_*. Each data set is binned in time intervals of 24 hr, each of which contains a maximum of 10 hrs of contiguous data.

Modeling the light curve based on the binary-lens interpretation is carried out in multiple steps. First, we conduct a preliminary grid search for the lensing parameters s, q, and α using the map-making method (Dong et al. 2006). In this process, the other lensing parameters are searched for by using a downhill approach. We set s, q, and α as grid parameters because the binary-lensing magnification varies sensitively to the change of these parameters, while the magnification varies smoothly to the changes of the other parameters. From the χ^2 map in the grid-parameter space obtained from this initial search, we then identify local minima. In the second stage, we refine each of the local minima by first refining the grid space and second by allowing all lensing parameters to vary. In the final stage, we compare the goodness of the identified local minima and find a global solution.

Deviations in binary-lensing light curves are mostly caused by either caustic approaches or crossings during which lensing magnifications are affected by finite-source effects. We account for the finite-source effect in computing finite-source magnifications using the inverse ray-shooting method (Kayser et al. 1986; Schneider & Weiss 1987) in the immediate neighboring region around caustics and using the semi-analytic hexadecapole approximation (Pejcha & Heyrovský 2009; Gould 2008) in the outer region surrounding caustics. In computing finite-source magnifications, we additionally consider the surface-brightness variation of the source star caused by limb darkening (Albrow et al. 1999) by modeling the surface brightness profile as

$$S_\lambda \propto 1 - \Gamma_\lambda \left(1 - \frac{3}{2}\cos\psi\right), \quad (2)$$

where Γ_λ is the limb-darkening coefficient and ψ is the angle between the normal to the surface of the source and the

line of sight toward the source. From the de-reddened color, it is found that the source is a G-type main-sequence star. See section 3.3 for the details of the source color measurement. Based on the source type, we adopt the limb-darkening coefficients $(\Gamma_V, \Gamma_R, \Gamma_I) = (0.74, 0.66, 0.57)$ from Claret (2000). For the MOA data, which are obtained from a non-standard filter system, we use $\Gamma_{RI} = (\Gamma_R + \Gamma_I)/2 = 0.62$.

In Table 1, we present the best-fit lensing parameters of the binary-lens solutions along with the χ^2 values per degree of freedom (dof). We find that the best-fit binary-lens model has two masses with a projected separation $s \sim 1.28$ and a mass ratio $q \sim 0.004$, which would make the companion a planetary-mass object projected near the Einstein radius of its host. The lens system induces two sets of caustics, where one (central caustic) is located close to the host and the other (planetary caustic) is located away from the host between the planet and the host. In Figure 1, we present the model light curve of the binary-lens solution in the region of anomaly. Also presented is the geometry of the lens system where the source trajectory with respect to the lens components (concave closed curves) is illustrated by a straight line with arrow head. We note that the source trajectory in the upper panel is aligned so that the data points marked on the trajectory match those on the light curve in the lower panel.

The fit in Figure 1 appears quite good. In particular, within the context of binary-lens models, the asymmetric peak by itself unambiguously indicates a low-mass companion aligned along the source trajectory, and it therefore unambiguously predicts an additional post-peak perturbation due to a planetary caustic. Such predictions were actually made in real time, just after the peak of the event and were seemingly confirmed by the late time "planetary" deviations. Moreover, there were at this time no known alternative class of physical effects that could induce a complex "planetary" light curve deviation of this type.

However, there were two important clues that this solution was not in fact correct. At first sight these appear to be independent, but are actually closely related. The first is that the normalized source size is very large $\rho_* = 8 \times 10^{-3}$ considering that the source is a dwarf. This would lead to a very small Einstein radius $\theta_{\rm E} \sim 0.05\,{\rm mas}$ and very small lens-source relative proper motion $\mu \sim 0.7\,{\rm mas\,yr^{-1}}$. These values are a priori unlikely, although not impossible: they could be generated by a very slow lens lying a distance $D_{\rm LS} \sim 20\,{\rm pc}(M/M_\odot)^{-1}$ in front of the source.

What raises this suspiciously large ρ_* to the level of implausibility is that it appears to be "driven" by the need to match basically smooth data to an intrinsically "bumpy" model. Because the source crossing time $t_* \equiv \rho_* t_{\rm E} \sim 5\,{\rm hr}$ is similar to the duration of an observing night, it is appropriate to bin these data by observatory and by day. Figure 2 compares these binned data to the best-fit model and also to the same model but with a more typical value of $\rho_* = 3 \times 10^{-3}$. This shows that the data are much smoother than the model for a typical ρ_* and are still considerably smoother than the model for the best-fit ρ_*. We therefore were led to consider what other physical effects might generate this "planetary" anomaly. [5]

3.2. *Binary-source Interpretation*

[5] In the Appendix, we present the results of modeling considering higher-order effects. We find that although these models improve the fit, there are still discrepancies with the data, and these models have their own problems as discussed in the Appendix.

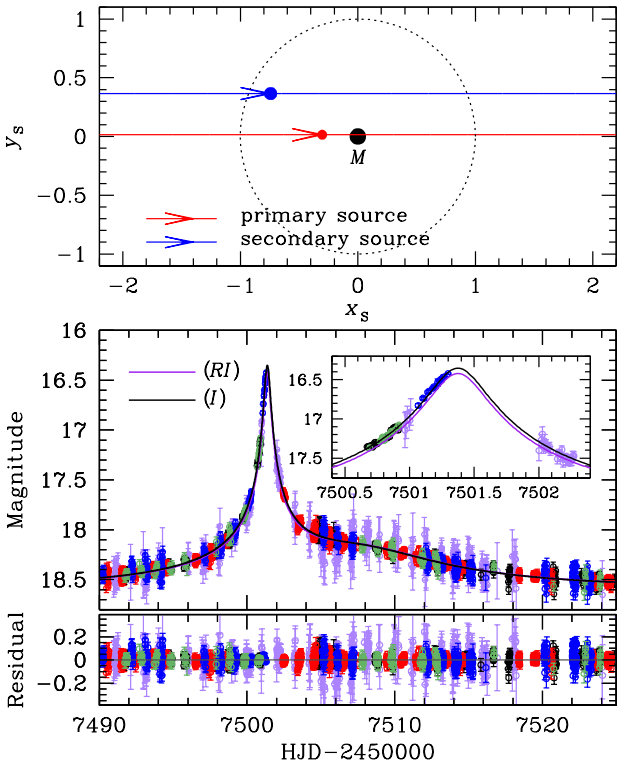

FIG. 3.— Geometry and light curve of the binary-source model. (1) The upper panel shows the geometry of the binary-source model. Two straight lines with arrows are the source trajectories of individual source stars. The lens is located at the origin (marked by *M*), and the dotted circle is the angular Einstein ring. The red and blue filled circles represent the individual source positions at HJD′ = 7497. Lengths are normalized by the Einstein radius. (2) The lower panel shows the enlarged view of the anomaly region. The two curves with different colors are best-fit binary-source models for *RI* and *I* passbands. The inset shows a zoom of the anomaly near HJD′ ∼ 7501.4.

We consider the possibility that the long-term deviation may be caused by a single-lens event with a binary source (binary-source event). The lensing magnification of a binary-source event corresponds to the flux-weighted mean of the magnifications of the two single-source events generated by the individual source stars (Griest & Hu 1992; Han 2002), i.e.

$$A = \frac{A_1 F_1 + A_2 F_2}{F_1 + F_2} = \frac{A_1 + q_F A_2}{1 + q_F}, \qquad (3)$$

where A_i denotes the lensing magnification of each source star with a flux F_i and $q_F = F_2/F_1$ is the flux ratio between the two source stars. The single-source magnification is related to the lens-source separation normalized to the angular Einstein radius, u_i, by

$$A_i = \frac{u_i^2 + 2}{u_i \sqrt{u_i^2 + 4}}; \qquad u_i(t) = \left[\left(\frac{t - t_{0,i}}{t_{\rm E}} \right)^2 + u_{0,i}^2 \right]^{1/2}, \qquad (4)$$

where $t_{0,i}$ is the moment of the closest lens approach to each source star, $u_{0,i}$ denotes the lens-source separation at that moment, and $t_{\rm E}$ is the time required for the source to cross the angular Einstein radius (Einstein time scale). [6] Therefore, one needs 6 principal parameters $(t_{0,1},\ t_{0,2},\ u_{0,1},\ u_{0,2},\ t_{\rm E},\ q_F)$

[6] We note that the individual single-source events share a common Einstein time scale because the transverse speeds of the two source stars with respect to the lens are same unless the orbital motion of the source is important.

for the description of a binary-source event. Since the flux ratio varies depending on the passband, one must add additional flux ratio parameters for each of the observed passbands.

We search for the solution of the binary-source parameters by a downhill approach. The initial values of the parameters are set based on the peak time, magnification, and duration of the event. For the χ^2 minimization of the downhill approach, we use the Markov Chain Monte Carlo (MCMC) method.

We find that the binary-source model is a good fit to the observed light curve. In Table 1, we list the best-fit parameters of the binary-source solution. In Figure 3, we present the geometry of the relative lens-source motion (upper panel) and the model light curve (lower panel) of the binary-source solution. In the upper panel, the two lines with arrows represent the trajectories of the two source stars with respect to the lens (marked by "*M*"). We designate the source passing closer to the lens as the "primary" source and the other source as the "secondary" source. We find that the flux ratio ($q_{F,RI}$ = 2.0 and $q_{F,I}$ = 1.9) is greater than unity, indicating that the source approaching closer to the lens is fainter than the source approaching farther from the lens. While binary-lens light curves are almost perfectly achromatic (after subtraction of the blended light), binary-source event light curves can be chromatic, implying that the magnification varies depending on the observed passband, and thus we present two model light curves corresponding to *RI* band (MOA) and *I* band (the other groups) data sets. According to the binary-source interpretation, the anomaly near the peak of the light curve was produced when the faint source star approached close to the lens and the anomaly in the declining wing was produced when the brighter source approached.

By comparing the binary-lens and binary-source interpretations, we find that the binary-source model better explains the observed light curve. The binary-source model improves the fit by $\Delta\chi^2 \sim 544$ compared to the binary-lens model. In Figure 4, we present the cumulative distribution of $\Delta\chi^2$ of the binary-source model with respect to the binary-lens model as a function of time. This shows that the improvements occurs during the strong anomaly near the peak and the declining part of the light curve after the peak. We find that the major improvement comes from KMTNet data which densely and continuously cover the anomaly throughout the event. The fit improvement from KMTNet data is $\Delta\chi^2 \sim 484$. On the other hand, the fit improvement from OGLE and MOA data, whose coverage of the anomaly is sparse and incomplete, are $\Delta\chi^2 \sim 10$ and 50, respectively. This demonstrates the importance of the high-cadence observation for the unambiguous characterization of the lensing event.

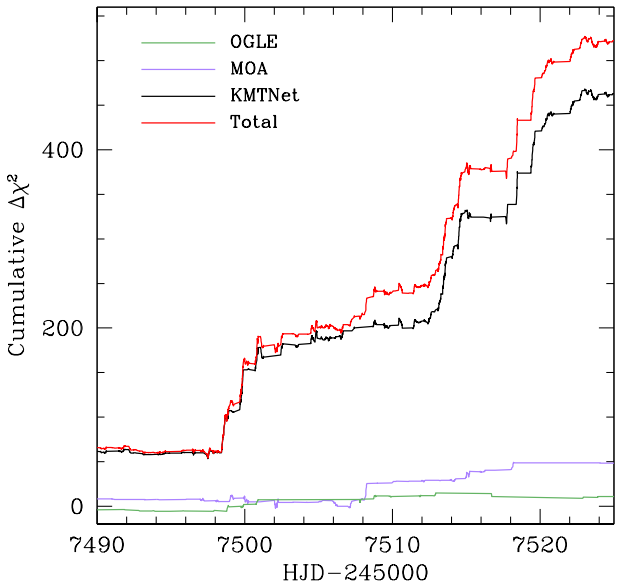

FIG. 4.— Cumulative distribution of χ^2 difference between the binary-source and binary-lens models.

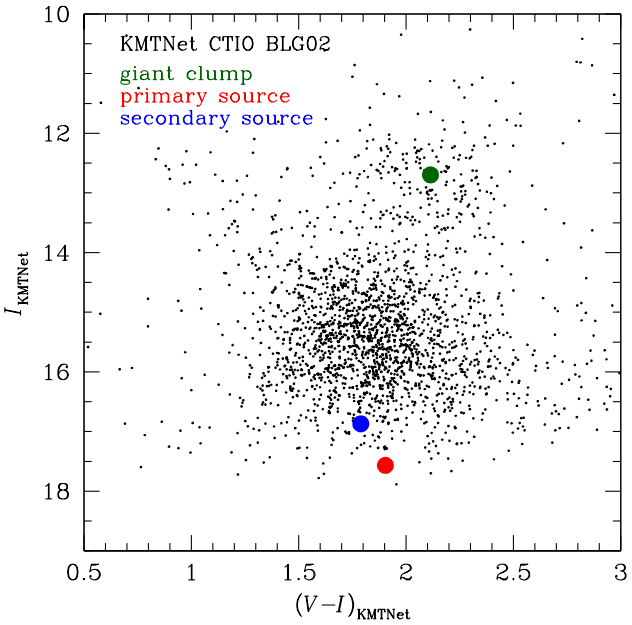

FIG. 5.— Instrumental color-magnitude diagram of stars in the region around the source stars. The positions of individual source components and the centroid of the giant clump are marked.

3.3. *Source Type*

Knowing that OGLE-2016-BLG-0733 is better explained by the binary-source interpretation, we characterize the individual source stars by estimating the source type based on the de-reddened color $(V-I)_0$ and brightness I_0. For this, we use four KMTNet pyDIA reductions ([CTIO+SAAO]×[BLG02+BLG42]) to construct the instrumental color-magnitude diagrams (CMD). Following the method of Yoo et al. (2004), we first estimate the offsets in color $\Delta(V-I)$ and magnitude ΔI of individual sources with respect to the centroid of giant clump (GC). Figure 5 shows the instrumental CMD of one of four KMTNet fields (CTIO BLG02) where the locations of individual sources and GC are shown. Under the assumption that the source and GC suffer the same extinction combined with the known de-reddened color and magnitude of GC, $(V-I,\ I)_{0,\rm GC}$ = (1.060, 14.433) (Bensby et al. 2011; Nataf et al. 2013), we then estimate the de-reddened color and magnitude of the individual sources. By applying this procedure to each KMTNet field, we find that the mean de-reddened color and magnitude of the individual sources are $(V-I,\ I)_{0,1}$ = (0.793, 19.322) for the primary and $(V-I,\ I)_{0,2}$ = (0.679, 18.626) for the secondary. These correspond to a late and an early G-type main-sequence star for the primary and the secondary, respectively.

Note that we also characterize the source star based on the binary-lens interpretation solely for the purpose of in-

corporating the limb-darkening coefficients into the binary-lens model. By following the same procedure, we determine the mean de-reddened color and magnitude of the source as $(V-I,\ I)_0 = (0.763,\ 19.601)$ corresponding to a G-type main-sequence star.

4. DISCUSSION

For the great majority of microlensing planets published to date (see Mróz et al. 2016 for a recent listing), the light curves exhibit sharp caustic crossings indicative of a binary lens. While in some cases there is difficulty in establishing whether the companion is planetary or has a more-equal mass ratio, this potential ambiguity is decisively resolved in almost all cases.

However, a high-cadence round-the-clock survey (similar to the KMTNet $\Gamma = 4\,\mathrm{hr}^{-1}$ fields) is capable of detecting much subtler planetary signals than those published to date. Furthermore, such a survey enables a complete statistical analysis that addresses all possible planetary signals rather than just individual detections. At the same time, Zhu et al. (2014a,b) have shown that of order half of the planets detectable will lack caustic crossing features. Hence, the problem of distinguishing such planetary light curves from other physical effects will be much more challenging than in the past, but extremely important for interpreting statistical results about planet populations.

Here we have presented the first of a new class of planet impersonators: roughly equal-luminosity binary source events, with the two sources being separated by substantially less than an Einstein radius. This can be regarded as a form of the degeneracy proposed by Gaudi (1998) in the sense that a binary source is masquerading as a planet. However, it lies quite far in parameter space from the original Gaudi degeneracy from the standpoint both of the physical nature of the binary source and the characteristics of the planetary light curve that are being imitated. For the Gaudi degeneracy, the second source is much fainter than the first and should be separated by of order an Einstein radius or more. In this way, the perturbation can appear to be short, and its symmetric form will not conflict with asymmetries of planetary perturbations generated by planets with projected separations near the Einstein ring. By contrast, the binary-source system of OGLE-2016-BLG-0733 has roughly equal brightness and so induces broad perturbations to the light curve, which are then confused with a broadened central peak and large planetary deviation, which are characteristic of a planet near the Einstein ring.

We found that, once binary-source models were investigated, it was quite easy to break this degeneracy, with $\Delta\chi^2 \sim 500$. Moreover, the planetary model exhibited "suspicious" behavior, which is what led us to investigate the binary source model. However, both of these means of distinguishing the two classes of models were dependent on having high-cadence data.

OGLE project has received funding from the National Science Centre, Poland, grant MAESTRO 2014/14/A/ST9/00121 to AU. The MOA project is supported by JSPS KAKENHI Grant Number JSPS24253004, JSPS26247023, JSPS23340064 and JSPS15H00781. Work by C. Han was supported by Creative Research Initiative Program (2009-0081561) of National Research Foundation of Korea. A. Gould acknowledges support from NSF grant AST-1516842. A. Gould was also supported by Korea Astronomy and Space Science Institute (KASI) grant 2016-1-832-01. The KMTNet telescopes are operated by the Korea Astronomy and Space Science Institute (KASI).

APPENDIX

BINARY-LENS MODELS WITH HIGHER-ORDER EFFECTS

Microlensing light curves are often subject to higher-order effects that cause subtle deviations from the form it would take based on rectilinear relative lens-source motion. One such effect is microlens parallax, which is caused by the change of the observer's position due to the orbital motion of Earth around the Sun (Gould 1992). Accounting for the parallax effect requires including two additional parameters $\pi_{\mathrm{E},N}$ and $\pi_{\mathrm{E},E}$ which are the two components of the microlens parallax vector $\boldsymbol{\pi}_{\mathrm{E}}$, projected onto the sky along the north and east equatorial coordinates, respectively (Gould 2004). The magnitude of the parallax vector corresponds to the ratio of the relative lens-source parallax $\pi_{\mathrm{rel}} = \mathrm{AU}(D_{\mathrm{L}}^{-1} - D_{\mathrm{S}}^{-1})$ to the angular Einstein radius, i.e., $\pi_{\mathrm{E}} = \pi_{\mathrm{rel}}/\theta_{\mathrm{E}}$, and its direction corresponds to the direction of the relative lens-source motion.

Another higher-order effect to be considered for the binary-lens case is the orbital motion of the lens (Dominik 1998; Albrow et al. 2000). The effect of the lens-orbital motion is two fold. First, the orbital motion causes the rotation of the binary axis, making the source motion deviate from rectilinear. Second, it also causes the binary separation to change in time, leading to a change in the caustic topology and thus of the magnification pattern around the caustic. To first-order approximation, the orbital motion of the lens can be parameterized as ds/dt and $d\alpha/dt$, which represent the change rate of the projected binary separation and the orientation angle, respectively.

Since there exist some residuals from the standard binary-lens model, we additionally test various models considering higher-order effects. In the "parallax" and "orbit" models, we separately consider the parallax effect and the orbital motion of the lens, while in the "parallax+orbit" model, we consider both the parallax and orbital effects.

We present the best-fit parameters considering higher-order effects in Table 2. We find that the higher-order effects improve the fit. The best-fit solution is the "parallax+orbit" model which improves the fit by $\Delta\chi^2 \sim 219$ from the standard binary-lens model. The major improvement occurs in the baseline and the caustic exits near $\mathrm{HJD}' \sim 7519$. However, the introduction of higher-order effects still does not provide a fully acceptable fit. In addition, considering that the anomaly lasted $\sim$30 days, the measured values of orbital parameters $(ds/dt,\ d\alpha/dt) = (-4.178,\ -11.715)$ are unusually large.

In order to check the validity of the "parallax+orbit" model, we evaluate the *projected* kinetic to potential energy ratio,

$$\left(\frac{\mathrm{KE}}{\mathrm{PE}}\right)_{\perp} = \frac{(r_{\perp}/\mathrm{AU})^3}{8\pi^2(M/M_{\odot})}\left[\left(\frac{1}{s}\frac{ds/dt}{\mathrm{yr}^{-1}}\right)^2 + \left(\frac{d\alpha/dt}{\mathrm{yr}^{-1}}\right)^2\right], \tag{A1}$$

TABLE 2
BINARY LENS: LENSING PARAMETERS

Parameters	Parallax	Orbit	Orbit+Parallax
χ^2/dof	12888.8/12345	12937.7/12345	12736.8/12343
t_0 (HJD′)	7501.551 ± 0.004	7501.569 ± 0.007	7501.587 ± 0.010
u_0	0.011 ± 0.001	0.011 ± 0.001	0.010 ± 0.001
$t_{\rm E}$ (days)	30.541 ± 0.576	30.375 ± 0.750	40.497 ± 1.763
s	1.247 ± 0.006	1.267 ± 0.018	1.364 ± 0.017
q (10^{-3})	2.778 ± 0.169	3.368 ± 0.358	3.871 ± 0.359
α (rad)	0.058 ± 0.002	0.058 ± 0.002	0.046 ± 0.004
ρ_* (10^{-3})	7.240 ± 0.248	7.037 ± 0.318	6.626 ± 0.336
$\pi_{{\rm E},N}$	-0.295 ± 0.441	–	6.983 ± 0.391
$\pi_{{\rm E},E}$	0.836 ± 0.126	–	2.163 ± 0.164
ds/dt (yr^{-1})	–	-0.094 ± 0.486	-4.178 ± 0.439
$d\alpha/dt$ (yr^{-1})	–	-0.285 ± 0.106	-11.715 ± 0.545

NOTE. — HJD′ = HJD − 2450000

which should satisfy $({\rm KE}/{\rm PE})_\perp < 1.0$ to be a stable system (Dong et al. 2009). Here $r_\perp = sD_{\rm L}\theta_{\rm E}$ is the physical projected separation between binary-lens components, $D_{\rm L} = {\rm AU}/(\pi_{\rm E}\theta_{\rm E} + \pi_{\rm S})$ is the distance to the lens, $M = \theta_{\rm E}/\kappa\pi_{\rm E}$ is the total mass of the binary-lens system, and $\pi_S = {\rm AU}/D_{\rm S}$ is the parallax of the source star. From the measured angular Einstein radius $\theta_{\rm E} = \theta_*/\rho_* = 0.058 \pm 0.005$ mas derived from the angular source radius $\theta_* = 0.382 \pm 0.027$ μas and the source radius ρ_*, we estimate that the total mass of the lens system is $M = (0.969 \pm 0.090) \times 10^{-3}\ M_\odot$ and distance to the lens is $D_{\rm L} = 1.834 \pm 0.134$ kpc. The measured ratio is then $({\rm KE}/{\rm PE})_\perp = 5.766$ and thus does not satisfy the boundedness condition. Therefore, the "parallax+orbit" model cannot be the solution of the event.

REFERENCES

Alard, C., & Lupton, Robert H. 1998, ApJ, 503, 325
Albrow, M. D., Beaulieu, J.-P., Caldwell, J. A. R., et al. 1999, ApJ, 522, 1022
Albrow, M. D., Beaulieu, J.-P., Caldwell, J. A. R., et al. 2000, ApJ, 534, 894
Albrow, M. D., Horne, K., Bramich, D. M., et al. 2009, MNRAS, 397, 2099
Bensby, T., Adén, D., Meléndez, J., et al. 2011, A&A, 533, 134
Bond, I. A., Abe, F., Dodd, R. J., et al. 2001, MNRAS, 327, 868
Bozza, V., Shvartzvald, Y., Udalski, A., et al. 2016, ApJ, 820, 79
Bramich, D. M., Horne, K., Albrow, M. D., et al. 2013, MNRAS, 428, 2275
Choi, J.-Y., Shin, I.-G., Han, C., et al. 2012, ApJ, 756, 48
Claret, A. 2000, A&A, 363, 1081
Dominik, M. 1998, A&A, 329, 361
Dong, S., Depoy, D. L., Gaudi, B. S., et al. 2006, ApJ, 642, 842
Dong, S., Gould, A., Udalski, A., et al. 2009, ApJ, 695, 970
Erdl, H., & Schneider, P. 1993, A&A, 268, 453
Gaudi, B. S. 1998, ApJ, 506, 533
Gaudi, B. S. 2012, ARA&A, 50, 411
Gould, A. 1992, ApJ, 392, 442
Gould, A. 2004, ApJ, 606, 319
Gould, A. 2008, ApJ, 681, 1593
Gould, A., & Loeb, A. 1992 ApJ, 306, 104
Gould, A., Yee, J. C., Bond, I. A., et al. 2013, ApJ, 763, 141
Griest, K., & Hu, W. 1992, ApJ, 397, 362
Han, C. 2002, ApJ, 564, 1015
Hwang, K.-H., Choi, J.-Y., Bond, I. A., et al. 2013, ApJ, 778, 55
Jung, Y. K., Udalski, A., Sumi, T., et al. 2015, ApJ, 798, 123
Kayser, R., Refsdal S., & Stabell, R. 1986, A&A, 166, 36
Kim, S.-L., Lee, C.-U., Park, B.-G., et al. 2016, JKAS, 49, 37
Mao, S., & Paczyński, B. 1991 ApJ, 517, L35
Mróz, P., Han, C., Udalski. A., et al. 2016, arXiv:1607.04919
Nataf, D. M., Gould, A., Fouqué, P., et al. 2013, ApJ, 769, 88
Paczyński, B. 1986, ApJ, 304, 1
Pejcha, O., & Heyrovský, D. 2009, ApJ, 690, 1772
Schneider, P., & Weiss, A. 1987, A&A, 171, 49
Sumi, T., Abe, F., Bond, I. A., et al. 2003, ApJ, 591, 204
Udalski, A. 2003, Acta Astron., 53, 291
Udalski, A., Szymański, M. K., & Szymański, G. 2015, Acta Astron, 65, 1
Woźniak, P. R. 2000, Acta Astron., 50, 42
Yee, J. C., Shvartzvald, Y., Gal-Yam, A., et al. 2012, ApJ, 755, 102
Yoo, J., DePoy, D. L., Gal-Yam, A., et al. 2004, ApJ, 603, 139
Zhu, W., Gould, A., Penny, M., Mao, S., & Gendron, R. 2014, ApJ, 794, 53
Zhu, W., Penny, M., Mao, S., Gould, A., & Gendron, R. 2014, ApJ, 788, 73